Temperature-dependent elasticity of B19′ NiTi; elastic softening and Elinvar effect

A. Ahadi[1,2*], R. Khaledialidusti[2], T. Kawasaki[3], S. Harjo[3], A. Barnoush[1] and K. Tsuchiya[1]

[1] International Center for Young Scientists, National Institute for Materials Science (NIMS), 1-2-1 Sengen, Tsukuba, Ibaraki 305-0047 (Japan).
[2] Department of Mechanical and Industrial Engineering, Norwegian University of Science and Technology (NTNU), Trondheim, Norway.
[3] J-PARC Center, Japan Atomic Energy Agency, 2-4 Shirane Shirakata, Tokai-mura, Naka-gun, Ibaraki 319-1195, Japan.

Abstract

The temperature-dependent elasticity behavior of the *B*19′ NiTi is unknown today. To gain insights into the lattice-level temperature-dependent elasticity of the *B*19′ crystal, we present results of *in-situ* neutron diffraction experiments performed on polycrystalline martensitic specimens in the temperature range of 300 down to 50 K. The experimental results are validated by the density functional theory molecular dynamics (DFT-MD) and Quasi Harmonic Approximation (QHA) calculations. The results show that the temperature-dependent Young's modulus (TDYM) of the B19′ crystal is strongly anisotropic. For different crystallographic orientations, the change in Young's modulus over the temperature range of 300-50 K ($\Delta E_{(hkl)} = E_{(hkl)}^{50K} - E_{(hkl)}^{300K}$) ranges from $\Delta E_{(10\bar{2})}$ = 2.8 ± 3.5 GPa (extremely weak) to $\Delta E_{(103)}$ = 59.6 ± 9.1 GPa (strong). A very weak elastic softening ($\Delta E_{(hkl)} < 0$) is observed in two of the orientations at 150 K. Two correlations are found between the TDYM and thermal expansion (TE) of each crystallographic orientation. First, the orientations with positive TE responses exhibit a stronger TDYM than the orientations with negative TE. Second, for orientations with positive TE the TDYM follows a Watchman-Varshni (exponential) trend, while the trend breaks down for the orientations with negative TE. The DFT-MD and QHA results capture qualitatively the highly anisotropic TDYM of the *B*19′ crystal and further show that there are orientations exhibiting elastic softening and ideally no change in Young's modulus ($\Delta E_{(hkl)}$ = 0) with cooling. This is found to originate from the negative temperature dependence of c_{35} compliance constant. The combined experimental and theoretical results help providing a unified scenario for the confluent Invar and Elinvar properties in shape memory alloys. It is proposed that these properties originate from the phonon properties of the B19′ crystal.

Keywords: Neutron diffraction; Anisotropic elasticity; Elastic Softening; Density functional theory; Invar and Elinvar

*Author to whom correspondence should be addressed; Aslan.Ahadi@ntnu.no

1. Introduction

Knowledge of the elastic properties of shape memory alloys (SMAs) is of critical importance in numerical modeling [1] and implementation of SMAs in aerospace [2], seismic [3], and biomedical applications [4]. In recent years, the researches on the elastic properties of NiTi SMAs have mostly focused on understanding the lattice-level elastic response of the martensite phase, which is comprised of B19′ (monoclinic) crystal structure [5–9]. In this regard, *in-situ* neutron diffraction studies have revealed a discrepancy between the macroscopic and lattice-level Young's modulus [5,6,8–12]. For the first time, Rajagopalan et al. [11] noticed a remarkable difference between the macroscopic Young's modulus (68 GPa) and lattice-level average Young's modulus of B19′ crystal (109 GPa) from neutron diffraction experiments. They ascribed such a difference to the onset of "twinning" at low stress levels of < 40 MPa. By employing a self-consistent polycrystalline model, Qiu et al. [8] showed the importance of elastic intergranular constraints and detwinning processes on the Young's modulus evolution. In a series of systematic studies, Stebner et al. [5,6] discussed the ability of texture-based analysis for evolution of Young's modulus. It was also shown that the orientation-specific Young's modulus (E_{hkl}) of B19′ crystal is highly anisotropic [10]. Sittner et al. [13] investigated the Young's modulus of B19′ crystal that is formed by stress-induced martensitic phase transformation from B2 phase. They argued that the low value of the Young's modulus that is widely reported in the literatures is "real" due to the unique anisotropy of the B19′ martensite [12,13].

Theoretical predictions by DFT calculations have confirmed the highly anisotropic nature of elastic modulus of B19′ crystal [7,14–16]. However, significant disparities between the DFT-predicted and experimentally-measured values of the E_{hkl} have been well-noted [7,8].

Among the several scenarios at play, Wang et al. [16] discussed the role of martensite microstructure (twinned vs single lattice) in correct interpretation of elastic moduli of B19′ crystal from DFT calculations. It has also been argued that the temperature-dependent elasticity of the B19′ crystal could be a source of the contradictory results [10]. This stems from the fact that the DFT calculations reveal the purely-elastic response of the B19′ lattice at 0 K [7,14–16], while the diffraction-based experiments provide the elastic responses of the B19′ in polycrystallie specimens at room temperature [5,6,8,10–12]. In an attempt to disclose the temperature-dependent elasticity of the B19′ lattice, Haskins et al. [17] calculated the temperature-dependent compliance constants $c_{ij}(T)$ over the temperature range of 50 to 600 K from DFT-MD calculations. From the experimental point of view, however, surveying the literature shows that the temperature-dependent elasticity of the B19′ is still unknown. The objective of this study is to unveil the temperature-dependent elasticity of the B19′ NiTi by combining *in-situ* low temperature neutron diffraction experiments with theoretical predictions.

The motive of this work is instigated by the ongoing reports of tailored TE (TTE) and weak TDYM (Elinvar effect) in thermomechanically-processed SMAs [18–21]. Ren et al. [22] proposed strain glass and the accompanying continuous phase transformation as the physical origin of TTE in SMAs. The other suggested proposal is that the TTE originates from the intrinsic anisotropic TE of the low symmetry crystals of the SMAs e.g., B19′ in NiTi [19], ordered tetragonal L10 in CoNiGa [18], and orthorhombic B19 in NiTiPd [18], which exhibit negative/positive/zero TE coefficients (CTE)s along different crystallographic orientations. However, little is known on the origin of Elinvar-like property in thermomechanically-processed SMAs [23]. One interesting observation is that the TTE and Elinvar properties generally accompany each other (i.e., they are confluent properties) [20,22,24]. Whether the Elinvar property is linked to the anisotropic TDYM of the B19′ crystal is unknown at the moment. In this paper, we first compare the experimental results of the TE of

the B19′ crystal with the theoretical predictions from our QHA, DFT-MD [17], and MEAM-MD simulations [25]. Then, the low temperature neutron diffraction results of TDYM of the B19′ crystal are presented. The experimental results are validated with the DFT-MD results published by Haskins et al. [17] and our QHA analysis. Finally, we discuss the origin of Invar and Elinvar properties in SMAs.

2. Experimental details

2.1 Material

The material used in our experiments is a slightly Ti-rich NiTi in the form of a rod provided by Fort Wayne Company. The alloy exhibits martensite finish temperature of M_f = 315 ± 3 K and hence it is fully martensitic at room temperature. The material is annealed at high temperatures and cooled under controlled condition so that martensite variants form randomly. The stress-strain responses of the material at three temperatures of 50, 150, and 300 K are shown in Fig. 1. It is seen that with decreasing temperature the stress plateau corresponding to reorientation of martensite variants increases from ∼ 214 MPa at 300 K to 562 MPa at 50 K [26]. The E calculated from the slope of the stress-strain curves in the very early stage of the deformation (dashed lines in Fig. 1) increases in an exponential fashion from 41.6 GPa at 300 K to 54.1 GPa at 50 K, as shown in the inset.

2.2 In-situ low temperature neutron diffraction experiments

In-situ neutron diffraction measurements are performed at the beam-line 19 (Takumi) of the Materials and Life Science Facility in the Japan Proton Accelerator Research Complex (J-PARC) using a high resolution time-of-flight neutron diffractometer [27]. The loading direction is oriented 45° to the direction of the incident beam. Diffracted spectra with diffraction vectors Q parallel and perpendicular to the loading direction are recorded at the north and south banks, respectively (Fig. 2(a)). Diffraction spectra are recorded for ∼ 30 min in the d-spacing range of 0.67 to 3.33 A˚. We have used a custom-built screw-driven

cryo-cooling loading frame that exploits a Gifford-McMahon technology [28,29] that is capable of reaching a nominal temperature of 6 K (see Fig. 2(b)). All diffraction spectra are collected under a high vacuum of better than 7.5×10^{-3} Pa. To measure the temperature of the specimen, a Chromel-Au/Fe(0.07 at.%) thermocouple is placed outside gauge section to avoid diffractions from the thermocouple. To allow for the temperature uniformity, the specimen is kept at the preset temperature for 5 hours. Measurements are performed at temperatures of 300, 150, and 50 K.

2.3 Specimens, loading, and temperature stability

Flat dogbone tensile specimens with a gauge length of 20 mm, thickness of 3 mm, and gauge width of 6 mm are used for neutron diffraction experiments (Fig. 2(c)). Indium foil is placed between the specimen and the jigs (made of copper-beryllium) to enhance the thermal contact [29]. Loading is performed in a stress-controlled mode at intervals of 10 MPa up to a maximum stress of 175 MPa at a stress rate of 1 MPa/min. After reaching each nominal stress level, the cross head displacement is kept constant allowing the stress relaxation during the collection of neutron diffraction spectra as it is shown in the inset of Fig. 2(d). The blue curve in Fig. 2(d) shows the temperature profile of the sample during the collection of the neutron spectra at a preset temperature of 50 K. It is seen that with loading the temperature of the gauge section rises by $\sim$ 0.5 K followed by a gradual decrease during the collection of neutron spectra. The average temperature profile fluctuates only by $\sim$ 1 K during the whole collection time of the neutron spectra, which indicates the high temperature stability of the system. The orientation-specific lattice strain ε_{hkl} for a given *hkl* plane reflection of B19′ crystal under macroscopic applied stress σ_{macro}, is calculated according to

$$\varepsilon_{hkl} = \frac{d_{hkl}^{\sigma_{macro}} - d_{hkl}^{0}}{d_{hkl}^{0}} \quad (1)$$

where d_{hkl}^{0} is the stress-free *d*-spacing of an *hkl* plane reflection and $d_{hkl}^{\sigma_{macro}}$ is the *d*-spacing under the applied macroscopic stress σ_{macro}. Note that due to stress relaxation during

collection of neutron spectra, the σ_{macro} is taken as the average stress.

2.4 Rietveld refinement

The recorded neutron spectra are refined using the Z-Rietveld code developed at the J-PARC. The code is based on nonlinear least-square algorithms, which enables successful application of Pawley method without requiring any constraints on the integrated intensities even in the case of severely overlapping peaks [30]. The crystal parameters used to refine the neutron spectra are as follow: space group of $P12_1/m$, lattice constants of a = 2.9002 Å, b = 4.1144 Å, c = 4.6540 Å, β = 97.7046°, atomic positions of x = 0.0372, y = 0.25, z = 0.1752 for Ni and x =0.4176 y = 0.25 z =0.7164 for Ti with the same anisotropic temperature factors of B11=B22=B33= 0.005 and B12=0.00067 for both elements. The neutron spectra are refined in the d-spacing range of 1.2-3.2 Å with a TOF function with cut off value of 0.1. A typical indexed neutron spectra is shown in Fig. 3.

3. Theoretical analysis

3.1 DFT calculations

First-principles calculations are performed using the Vienna *Ab-initio* Simulation Package (VASP) [31,32]. The generalized gradient approximation (GGA) using the Perdew-Bruke-Ernzerhof (PBE) functional is applied for the exchange correlation [33,34]. A Conjugate gradient scheme is employed with an iterative relaxation of the atomic positions with the residual forces acting on the atoms of 0.01 eV/Å and a total energy convergence of 10^{-6} eV per unit cell. A planewave cutoff energy of 500 eV and a 15×11×10 Monkhorst−Pack [32] k-point mesh are examined for the Brillouin zone sampling of a 1×1×1 supercell of NiTi. Thermal properties and temperature-dependent lattice constants of NiTi are studied by density functional perturbation theory (DFPT) [35,36]. The phonon dispersions are calculated by the PHONOPY code [37,38] within a 4×3×2 supercell of NiTi including 96 atoms (48 Ni and 48

Ti) with k-point meshes of 4×3×5 Monkhorst−Pack [32].

3.2 Temperature-dependent lattice constants of B19′ crystal

In order to calculate the temperature-dependent lattice constants of the B19′ crystal we have employed and improved the approach introduced by Won Seok [39]. The approach starts with optimization of lattice parameters *a*, *b*, and *c* for a fixed monoclinic angle β from 90^o to 108^o. Since the structure optimization with a fixed β is not implemented in the standard VASP code, we applied an optimization technique presented by Mizuno et al.[40]. To capture the temperature effect on the lattice constants, the energy landscapes between the B19, B19′, and B33 structures as a function of the monoclinic angle β at different temperatures is calculated by QHA. It is important to note that in the previous work [39], a harmonic approximation analysis has been employed. In this study, we have employed QHA method taking into account the anharmonic volume dependence of the phonon properties.

3.3 Temperature-dependent compliance constants $c_{ij}(T)$ of B33 and B19′

Here we briefly describe the method that we employed for calculating the $c_{ij}(T)$ of the *B33* and *B19′* crystals. Details of the calculations are found in Refs. [41,42]. Isothermal $c_{ij}(T)$ can be considered as strain derivatives of the Helmholtz free energy *F* [41]:

$$F[X(\zeta);T] = E[X(\zeta)] + F_{\text{vib}}[X(\zeta);T] \quad (2)$$

where $E[X(\zeta)]$ is the total energy of the specific deforming configuration. $F_{\text{vib}}[X(\zeta);T]$ is the vibrational Helmholtz free energy calculated from phonon density states. There are 13 independent elastic constants c_{11}, c_{22}, c_{33}, c_{44}, c_{55}, c_{66}, c_{12}, c_{13}, c_{15}, c_{23}, c_{25}, c_{35}, and c_{46} for a *B19′* crystal. To calculate $c_{ij}(T)$, 14 sets of deformed crystals are required, which can establish 14 sets of Helmholtz free energy $F[X(\zeta);T]$ curves with respect to strain ζ at given temperatures. We chose $(\zeta, \zeta, \zeta, 0, 0, 0)$, $(\zeta, -\zeta, \zeta^2/(1-\zeta^2), 0, 0, 0)$, $(\zeta, \zeta^2/(1-\zeta^2), -\zeta, 0, 0, 0)$, $(\zeta, \zeta, 0, 0, 0, 0)$, $(\zeta, 0, \zeta, 0, 0, 0)$, $(0, \zeta, \zeta, 0, 0, 0)$, $(\zeta^2/(1-\zeta^2), \zeta, -\zeta, 0, 0, 0)$, $(\zeta^2/(1-\zeta^2), 0, 0, 2\zeta, 0, 0)$, $(\zeta, 0, 0, 0, 2\zeta, 0)$, $(\zeta, 0, 0, 0, -2\zeta, 0)$, $(0, \zeta, 0, 0, 2\zeta, 0)$, $(0, 0, \zeta, 0, 2\zeta, 0)$, $(0, 0, 0, \zeta, 0, \zeta)$ and $(0, 0, 0, \zeta, 0, -\zeta)$) as 14

deformation modes. For the space consideration, further details of the calculations are left to the readers [41].

4. Results and discussion

4.1 TE behavior of B19′ crystal; comparison of the neutron diffraction data with the theoretical predications

Let us start with a comparison between the measured TE behavior of the B19′ crystal from neutron diffraction experiments (Fig. 4(a)), with those predicted from our QHA analysis (Fig. 4(b)), DFT-MD results of Ref. [17] (Fig. 4(c)), and MEAM-MD results of Ref. [43] (Fig. 4(d)). The first row in Fig. 4(a) shows the thermal strain evolution of sixteen *hkl* planes of the B19′ crystal during cooling from 300 down to 50 K. The thermal strain is calculated as $\frac{d_{hkl}^{T}-d_{hkl}^{300K}}{d_{hkl}^{300K}} \times 100$ where d_{hkl}^{T} is the *d*-spacing at a temperature *T* and d_{hkl}^{300K} is the *d*-spacing at a reference temperature of 300 K. The error bars in Fig. 4(a) are associated with the statics of peak fitting. In line with the previous reports [9,19], the measurements show that the B19′ crystal exhibits orientations with both positive and negative TE responses. The orientations perpendicular to 100, 102, 112, 120, 020, 021, 103, $12\bar{1}$, and 011 planes are the positive TE orientations, while $11\bar{1}$, $12\bar{2}$, $10\bar{1}$, 002/003, $11\bar{2}$ and $10\bar{2}$ are the negative ones. From these measurements and using a least-square approach [44], the four components of the TE matrix at 300 K are calculated as α_{11} = 19.7 ×10^{-6} K^{-1}, α_{22} =27.3 ×10^{-6} K^{-1}, α_{33} = -18.8×10^{-6} K^{-1}, and α_{13} = 40.3×10^{-6} K^{-1}. A detailed description of the calculations can be found in Ref. [10,18,19]. The three dimensional representation surface of the TE matrix is shown in the second row of Fig. 4(a). The blue dumbbell represents a set of crystallographic orientations that exhibit negative TE responses and the yellow torus represents the set of crystallographic orientations with

positive TE.

Comparing the neutron diffraction results with the theoretical predictions in Fig. 4(b-d), it is seen that the QHA, DFT-MD, and MEAM-MD results can all qualitatively capture the strongly anisotropic TE nature of the B19′ crystal. However, our QHA results capture a non-linear evolution of the thermal strain with temperature, as observed in the experiments, while, the DFT-MD [17] and MEAM-MD [43] give a linear dependence. Quantitatively speaking, the CTE values predicted from the MEAM-MD are significantly larger than the experimental results. In Fig. 3(a) it is seen that the orientation perpendicular to 100 plane is a strong positive TE plane; however, the QHA, DFT-MD, and MEAM-MD results all predict that this orientation is a weak positive TE plane. In agreement with the experimental observations, the orientation perpendicular to 020 plane is predicted as strong positive TE plane in DFT-MD and MEAM-MD results, which is not accurately captured in our QHA analysis. The 002 plane, is a medium negative TE plane and is accurately captured with the DFT-MD results. Consequently, overall better agreement is observed between the DFT-MD results of Haskin et al. [17] with our experiments. As a concluding remark, the above comparisons show that the available theoretical predictions on the temperature-dependent lattice constants and the ensuing anisotropic TE behavior of the B19′ crystal can qualitatively capture the experimental observations. Further theoretical advancements toward quantitative accuracies are desired.

4.2 Orientation-specific elasticity of B19′ NiTi at room temperature; comparison with previous studies

The black markers in Fig. 5 show the evolution of lattice strain ε_{hkl} with σ_{macro} along the loading direction for 15 different *hkl* plane reflections of the B19′ crystal at 300 K. Note that due to the relaxation of stress in the course of collecting neutron spectra (inset of Fig. 2(d)), the σ_{macro} represents the average stress in each cycle. The error bars are associated with the statistics of peak fitting and the dashed lines represent linear fits to the σ_{macro} vs.

ε_{hkl}, for $\sigma_{macro} \leq$125 MPa, which is used to extract the E_{hkl} (=$\sigma_{macro}/\varepsilon_{hkl}$). It is worth mentioning that compared with the previous studies [8,10,11], we have recorded neutron spectra at smaller stress intervals that results in statistically more reliable values of E_{hkl}. Furthermore, the enhanced detector system of the Takumi beamline enables acquiring sharper peaks with better resolution and higher signal to noise ratio, which is beneficial for study of the B19′ crystal with overlapping peaks. For example, as it was seen in Fig. 3, peak numbers 6 and 7 ($10\bar{2}$ and 021) are well-separated, while they are overlapped in Ref. [5]. The 120 and 102 peaks are fully overlapped in Ref. [5] and hence, their E_{hkl} values are not reported. However, as it is seen in Fig. 3, these peaks are relatively separated and the *d*-spacing of each peak can be satisfactorily refined.

As it is seen in Fig. 5, despite the nonlinear stress-strain behavior of the polycrystalline specimen at 300 K (see Fig. 1), the σ_{macro} vs. ε_{hkl} appears linear for most of the *hkl* planes up to 125 MPa. For 102 and 112 peaks deviations from linearity is observed at $\sigma_{macro} \geq$ 125 and 150 MPa, respectively. In Table 1, the values of E_{hkl} at 300 K are compared with the previous reports [8,10]. A relatively good agreement is noted for some of the orientations. For example, for orientation perpendicular to 011 plane E_{011} = 113.1 GPa, which is the same as the reported value of 113 GPa by Rajagopalan et al. [11] and close to 117.1 GPa by Qiu et al. [8]. For other orientations such as perpendicular to $10\bar{1}$ plane, we have measured *E* of 67.2 GPa, which lies in between the reported values by Stebner et al. (65.2 GPa) and Qiu et al. (78.2 GPa). Overall, our measured values are in closer agreement with the Qiu et al [8]. It is worth noting that Qiu et al. [8] reported E_{120} = 167.1 GPa and $E_{10\bar{1}}$ = 78.2 GPa as the highest and lowest values of the Young's modulus. Here, we have measured E_{020} = 183.5 GPa as the highest and $E_{10\bar{1}}$ = 67.2 GPa as the lowest values, which indicate stronger anisotropy of the Young's modulus of *B19′* NiTi than the previous reports [8,10].

4.3 Temperature-dependent Young's modulus (TDYM) of B19′ crystal; comparison with 0 K

self-consistent polycrystalline models

In Fig. 5, the red and blue markers/dashed-lines represent the evolution of ε_{hkl} with σ_{macro} at temperatures of 150 and 50 K, respectively. As expected, with decreasing temperature the slope of the dashed lines (E_{hkl}) increases for most of the orientations[1]. However, it is evident that such increase in E_{hkl} is highly orientation-specific. A visual inspection of the slopes in Fig. 5 shows that for some orientations such as perpendicular to 102 (peak 9), 103 (peak 15), and 112 (peak 12) planes, E_{hkl} is strongly temperature sensitive, while for some orientations such as perpendicular to $10\bar{1}$ (peak 3), $12\bar{2}$ (peak 8), and $10\bar{2}$ (peak 9) planes such increase is relatively weak. Fig. 6 summarizes the variations of E_{hkl} with temperature. The strongest TDYM is observed in the orientation perpendicular to 103 plane where E increases from 107.5 ± 2.8 GPa at 300 K, to 152.1 ± 9 GPa at 150 K, and further to 167.1 ± 9.1 GPa at 50 K corresponding to ΔE = 59.6 GPa over the whole tested temperature range. The orientation perpendicular to $10\bar{2}$ plane exhibits the weakest TDYM where E initially decreases from 84.6 ± 1.1 GPa at 300 K, to 81.8 ± 2.1 GPa at 150 K, and further increases to 87.4 ± 3.5 GPa at 50 K corresponding to an extremely weak change of ΔE = 3.3 ± 4.3 % over temperature range of 300 to 50 K.

Before further expansion of the experimental results, let us point to a meaningful trend that highlights the accuracy of our measurements. Consider as an example the 102 (peak 15) and 103 (peak 9) planes with d-spacings of 1.694 A˚ and 1.288 A˚, respectively. The normals to these planes lie in the a-c plane of the B19′ crystal and the angular difference between them is 9.6˚. Thus, these two orientations are expected to have close values of E at 300 K as well as similar TDYM behaviors. Despite having different Pearson linear correlation coefficients (ρ) associated with the Rietveld refinement (102 plane has a much stronger intensity than the 103 plane), both orientations appear to have close values of E_{hkl} at 300 K (E_{102} = 92.3 GPa and E_{103}

[1] For the orientations perpendicular to $12\bar{2}$ and $10\bar{2}$ planes, the E_{hkl} decreases a little with cooling from 300 to 150 K (i.e., elastic softening occurs) and it increases slightly with further cooling down to 50 K.

= 107.3), and they exhibit strong TDYM. Moreover, the mode of TDYM follows a similar exponential trend for both orientations as it is seen in Fig. 6. Similarly, $E_{10\bar{1}}$ = 69.5 GPa and $E_{10\bar{2}}$ = 84.6 GPa and both orientations show a very weak TDYM and the mode of TDYM follows a non-exponential trend.

Qiu et al. [8] employed a self-consistent polycrystalline model and showed a much higher agreement with the neutron diffraction results, compared with the single crystalline DFT predictions, however, the role of temperature has not been discussed. Comparing our 50 K results with the E_{hkl} from self-consistent model (see Table 2), it is observed that for some orientations such as 011, $11\bar{1}$, $11\bar{2}$, $12\bar{1}$, better agreements are obtained, while for some orientations the values of E_{hkl} at 50 K are higher than the self-consistent predictions. This points to the fact that any realistic model should not only take into account the inelastic contributions, but also the highly anisotropic temperature-dependent elasticity of the *B19′* crystal has to be considered.

4.4 Correlations between TDYM and CTE and breakdown of the Watchman-Varshni equation

As it is clearly seen in Fig. 6, the orientations with positive TE responses show, overall, a stronger TDYM than the orientations with negative TE. Comparing the TDYM within the orientations with positive TE, it is seen that those sets of orientations with higher values of CTE exhibit stronger TDYM than the orientations with lower values CT[2]. For example, the orientations perpendicular to 103, 102, 112, and 020 planes with the largest values of CTE exhibit the strongest TDYM. The orientations perpendicular to $12\bar{1}$ and 011 planes with the lowest values of CTE, exhibit the weakest temperature sensitivity. Comparing the TDYM of the orientations with negative TE responses, no systematic dependence to CTE is observed as orientations perpendicular to $10\bar{2}$ (CTE = -26.1×10^{-6} K^{-1}), and $12\bar{2}$ (CTE = -4.6×10^{-6} K^{-1}), and $10\bar{1}$ (CTE = -11.3×10^{-6} K^{-1}) planes, all exhibit extremely weak TDYM. The results in Fig.

[2] The orientation perpendicular to 120 plane seems an exception. Despite having a large positive CTE (19.7×10^{-6} K^{-1}), this orientation shows a moderate TDYM.

6 further show that there is a distinct difference in the mode of TDYM between the orientations with positive and negative TE responses. In the positive TE orientations, the E_{hkl} increases rather considerably with decreasing temperature to 150 K and tends to saturate with further decrease of temperature to 50 K. Such temperature dependence follows the empirical equation (exponential) proposed by Watchman and Varshni [45] as follow:

$$E_{hkl}(T) = E_{hkl}^{0K} - BTexp(-\frac{T_0}{T}) \quad (3)$$

where T is temperature, E_{hkl}^{0K} is the orientation specific Young's modulus at 0 K, and B is a constant. In contrast, for the orientations with negative TE responses, the E_{hkl} increases rather insignificantly with decreasing temperature to 150 K and further increases noticeably down to 50 K. This shows that the Watchman-Varshni equation breaks down to fit the TDYM of the orientations with the negative TE responses.

4.5 DFT-MD and QHA results of TDYM

Haskins et al. [17] calculated the temperature-dependent compliance constants $c_{ij}(T)$ of the $B19'$ and $B33$ crystal structures of the NiTi using a modified version of thermodynamic upsampling within DFT-MD calculations. We have calculated the orientation-dependent Young's modulus of the $B19'$ and $B33$ crystal structures from the $c_{ij}(T)$ data provided by Haskins et al. [17] using MTEX Toolbox [46]. Fig. 7(a) illustrates the three dimensional representation surfaces (quadric)s of the Young's modulus at two temperatures of 300 and 50 K for $B19'$ crystal. These surfaces characterize the variation of Young's modulus along different crystallographic orientations at 300 and 50 K. Note that the quadrics have two-fold symmetry along the Y (b of the B19′) axis. It is seen that with a decrease of temperature the quadric expands. It is also clear that such expansion is non-uniform and the overall shape of the quadric varies, which hints at the anisotropy of the TDYM of the B19′ crystal. The anisotropic TDYM is better illustrated in two-dimensional cross-section plots, as they are shown in Fig. 7(b) for five selective planes rotated by different angles around the Y axis. For planes 1 and 5, the

TDYM is realized by a relatively-isotropic/weakly-anisotropic TDYM, where with a decrease of temperature E_{hkl} increases ($\Delta E > 0$) along all crystallographic orientations. In the plane number 2, the TDYM is anisotropic. The red dashed lines define a set of crystallographic orientations where TDYM is very weak ($\Delta E \sim 0$) as opposed to Y direction ([010]) where the TDYM is strong and positive $\Delta E > 0$. In the planes 3 and 4, a range of crystallographic orientations (blue dashed lines) appear to exhibit negative TDYM (elastic softening) where with a decrease of temperature E_{hkl} decreases ($\Delta E < 0$). The intersection between the orientations that exhibit $\Delta E < 0$ and $\Delta E > 0$ responses, characterize a set of crystallographic orientations at which an ideal Elinvar ($\Delta E = 0$) exists. Another prediction from the DFT-MD results that is close to our experimental observations (see Fig. 6) is that the orientations that exhibit $\Delta E \sim 0$ and $\Delta E < 0$ responses, appear to possess lower values of the Young's modulus compared to orientations with $\Delta E > 0$. It should be note that in our experiments we did not observe any orientation that exhibits $\Delta E < 0$ in the whole temperature range of 300 to 50 K. We only noticed that the orientations with low values of Young's modulus, such as perpendicular to $11\bar{2}$ (E_{300K} = 86.3 GPa), $10\bar{2}$ (E_{300K} = 84.6 GPa), and $10\bar{1}$ (E_{300K} = 69.56 GPa) planes, they all exhibit weak TDYMs $\Delta E \sim 0$. Note that for $10\bar{2}$ and $10\bar{3}$ plane, with a high Pearson linear correlation coefficient, we noted a small decrease in the Young's modulus with a decrease of temperature down to 150 K (blue arrows in Fig. 6).

We have calculated the evolution of the orientation-specific Young's modulus with temperature $E_{\mathrm{hkl}}(T)$ for some orientations of positive and negative TE responses using the following equation [44]:

$$\frac{1}{\mathrm{E}_{hkl(T)}} =$$

$$l_1{}^4 s_{11(T)} + 2l_1{}^2 l_2{}^2 s_{12(T)} + 2l_1{}^2 l_3{}^2 s_{13(T)} + 2l_1{}^3 l_2 s_{15(T)} + l_2{}^4 s_{22(T)} + 2l_2{}^2 l_3{}^2 s_{23(T)} +$$

$$2l_1 l_2{}^2 l_3 s_{25(T)} + l_3{}^4 s_{33(T)} + 2l_1 l_3{}^3 s_{35(T)} + l_2{}^2 l_3{}^2 s_{44(T)} + 2l_1 l_2{}^2 l_3 s_{46(T)} + l_1{}^2 l_3{}^2 s_{55(T)} +$$

$$l_1^{\,2} l_2^{\,2} s_{66(T)} \quad (4)$$

where l_1, l_2, and l_3 are the direction cosines normal to an *hkl* plane of the B19′ crystal and $s_{ij}(T)$ is the stiffness tensor (i.e., the inverse of the compliance matrix $c_{ij}(T)^{-1}$). As it is seen in Fig. 7(c), the DFT-MD results predict the highly anisotropic nature of the B19′ crystal, however, it predicts a Watchman-Varshni trend for all the positive and negative TE orientations (i.e., it fails to capture the non-exponential trend that we observed in all negative TE orientations). Moreover, the strongest TDYM from DFT-MD calculations were determined to be $\Delta E = 31$ GPa, which is almost half of the ΔE of the orientation perpendicular to 103 plane with the highest sensitivity of E to temperature (see Fig. 6). These quantitative discrepancies indicate that there is still advancement desired toward fabrication of single crystalline B19′ specimens and conducting low temperature neutron diffraction observations.

Before discussing the temperature-dependent elasticity of the *B*19′ crystal from our QHA analysis, it is important to bring in mind that the calculation of $c_{ij}(T)$ of the *B*19′ crystal from QHA is not reliable, since the B19′ is not the ground-state structure of the NiTi at 0 K. Being aware of such limitation, we performed QHA calculations on the *B*33 and *B*19′ crystals and calculated the $c_{ij}(T)$ for both crystals. Fig. S1 summarizes the temperature-dependent elasticity behavior of the B19′ crystal from our QHA analysis. Surprisingly, the QHA calculations yields qualitatively similar results as that of the DFT-MD; it captures the existence of crystallographic orientations with $\Delta E > 0$, $\Delta E < 0$, and ideal Elinvar ($\Delta E = 0$). Moreover, the non-exponential TDYM is also captured with QHA. This is an interesting finding since our QHA analysis captures the non-linear TE behavior as well, unlike the DFT-MD and MEAM-MD results that predict linear dependencies (see Fig. 4). Furthermore, from our QHA calculations and DFT-MD results of Haskins et al. [17], we noted that the "hypothetical" *B*33 crystal structure does not show orientations with negative/zero TE, nor orientations that undergo elastic softening during cooling (results are not shown). Comparing the $c_{ij}(T)$ data of

the $B33$ and $B19'$ crystals, we found that it is the strong negative temperature-dependence of the c_{35} compliance constant that brings the $\Delta E < 0$, $\Delta E \approx 0$, and $\Delta E = 0$ to the temperature-dependent elasticity behavior of the $B19'$ crystal.

Finally, although several experimentally-observed features of the temperature-dependent elasticity of the $B19'$ crystal are captured qualitatively with QHA and DFT-MD calculations, the theoretically-predicted elastic softening over the whole tested temperature range (300 down to 50 K) was not observed in our experiments. This might be due to the fact that the range of crystallographic orientations that show elastic softening $\Delta E < 0$ are narrower than the orientations with $\Delta E > 0$ and thus more difficult to detect. It may also be attributed to the temperature-dependence of twin boundary motions in our polycrystalline specimens.

4.6 Mechanism of Elinvar and Invar in nanocrystalline SMAs

By surveying the literature, it is revealed that the Elinvar and Invar (more precisely tailored TE) are the two confluent properties that come together in most studied nanocrystalline SMA systems. For example, we observed tailored TE [19] and invariance of superelasticity with temperature down to 18 K (Elinvar) [29] in a severely-deformed superelastic NiTi. Multifunctional Gum metal [24], NiTiFe [20], and TNTZ-1.2O [22] are typical SMAs that exhibit the confluent Invar and Elinvar properties. To the best of our knowledge, there is no consensus on the origin of these nascent properties in SMAs. One of the proposed scenarios is that both Invar and Elinvar originates from the continuous phase transformation upon cooling [22,47]. Such proposed mechanism, however, fails to explain the tailored TE observed in fully martensitic SMA systems, where no continuous/discontinuous phase transformation occurs with cooling [18]. Monroe et al. [18] proposed that the tailored TE leading to Invar effect in SMAs, originate from the anisotropic TE of the low symmetry crystals of SMAs [18]. We also showed that the tailored TE in severely-rolled sheets originate from intrinsic TE of the

stabilized $B19'$ crystal. The close agreement between DFT-MD, QHA, and experimental results presented in Fig. 4 to Fig. 7 help providing a unified mechanism, based on the phonon properties of the B19′ crystal, for the confluent Elinvar and Invar properties in SMAs. The results clearly show that the $B19'$ crystal exhibits the negative/positive/zero TE as well as negative/positive/zero TDYM along different crystallographic orientations. Lastly, the reports on Elinvar effect in SMAs show that a low value of Young's modulus remain invariant with temperature e.g., ~ 60 GPa for Gum metal [24], ~45 GPa for TNTZ-1.2O [22], and ~50 GPa for NiTiFe [47]. Our neutron diffraction experiments, DFT-MD, and QHA results (Fig. 6, Fig. 7, and Fig. S1), all show that those orientations with low values of Young's modulus exhibit a weak TDYM. We believe these observations are complelling evidence that Invar and Elinvar in SMAs originate from the phonon properties of B19' crystal.

6. Summary and conclusions

We have investigated the temperature-dependent elasticity behavior of the $B19'$ monoclinic NiTi in polycrystalline specimens over the temperature range of 300 to 50 K, using time-of-flight neutron diffraction experiments. For the first time, the temperature-dependent Young's modulus (TDYM) of different crystallographic orientations ($E_{\mathrm{hkl}}(T)$) is measured. To validate the experimental findings, Quasi Harmonic Approximations (QHA) and density functional theory molecular dynamics (DFT-MD) calculations are employed. From the experimental and theoretical findings the following conclusions are drawn:

1. The orientation-specific temperature-dependent Young's modulus (TDYM) of unique 15 crystallographic orientations in the $B19'$ crystal are measured. It is shown that the TDYM of the $B19'$ crystal is strongly anisotropic. The change in Young's modulus over the temperature range of 300 to 50 K ($\Delta E_{hkl} = E_{hkl}^{50K} - E_{hkl}^{300K}$) varies from extremely weak

with $\Delta E_{10\bar{2}}$ = 2.8 ± 3.5 GPa, for an orientation perpendicular to $10\bar{2}$ plane, to very strong with ΔE_{103} = 59.6 ± 9.1 GPa, for an orientation perpendicular to 103 plane.

2. By comparing the measured values of E_{hkl} at 50 K with the single crystalline DFT and self-consistent polycrystalline models, it is found that the temperature effect is not the main reason for the discrepancies between the theoretical and experimental results of E_{hkl}. Instead, the intergranular stresses and martensite morphology (twinned vs. detwinned) seem to play major roles.

3. Two correlations are found between the thermal expansion (TE) behavior and TDYM of each crystallographic orientation. First, the orientations with positive TE responses exhibit an over-all stronger TDYM than the orientations with negative TE responses. Second, in the orientations with positive TE the TDYM follows the Watchman-Varshini type (exponential) trend. The Watchman-Varshini trend breaks down in the orientations with negative TE, which leads to much weaker TDYM compared with the positive TE orientations.

4. From the temperature-dependent compliance constants obtained from DFT-MD and QHA calculations, the TDYM of the $B19'$ crystal is calculated and represented in three dimensions. The $B19'$ NiTi comprises crystallographic orientations that exhibit elastic hardening ($\Delta E > 0$), anomalous elastic softening ($\Delta E < 0$), as well as orientations with ideally zero TDYM ($\Delta E = 0$). In contrast, the "hypothetical" $B33$ crystal only shows orientations with $\Delta E > 0$. It is found that the negative and weak TDYM of the B19′ crystal originates from the negative temperature dependence of c_{35} compliance constant.

5. Our experimental findings along with the theoretical calculations indicate that the nascent Elinvar and Invar properties in SMAs both originate from the phonon properties of the $B19'$ crystal.

Acknowledgments

This work is financially supported by International Center for Young Scientists (ICYS) under grant number C1052. Partial supports from JSPS Kakenhi 15H05767 are appreciated. We would like to thank Dr. Jeremy Schaffer from Fort Wayne for providing the polycrystalline specimens. We thank Kono Kenichiro for valuable discussions and insightful comments on low temperature experiments. Cryogenic neutron diffraction measurements were performed through project number 2018B0042 at MLF of J-PARC. We thank Dr. Justin Haskins and Dr. John Lawson from NASA Ames Research Center for providing the hard data of their temperature-dependent compliance constants. We also thank Jan Inge Hammer Meling and Qiao Li from Wuhan University for assistance with plotting elasticity matrix in MTEX. We acknowledge the financial support from VISTA of The Norwegian Academy of Science and Letters.

References

[1] A.P. Stebner, S.C. Vogel, R.D. Noebe, T.A. Sisneros, B. Clausen, D.W. Brown, A. Garg, L.C. Brinson, Micromechanical quantification of elastic, twinning, and slip strain partitioning exhibited by polycrystalline, monoclinic nickel-titanium during large uniaxial deformations measured via in-situ neutron diffraction, J. Mech. Phys. Solids. 61 (2013) 2302–2330. doi:10.1016/j.jmps.2013.05.008.

[2] D.J. Hartl, D.C. Lagoudas, Aerospace applications of shape memory alloys, Proc. Inst. Mech. Eng, Part G J Aerosp. Eng. 221 (2007) 535–552. doi:10.1243/09544100JAERO211.

[3] S. Saadat, J. Salichs, M. Noori, Z. Hou, H. Davoodi, I. Bar-on, Y. Suzuki, A. Masuda, An overview of vibration and seismic applications of NiTi shape memory alloy, Smart Mater. Struct. 11 (2002) 218–229. doi:10.1088/0964-1726/11/2/305.

[4] T. Duerig, A. Pelton, D. Stockel, An overview of nitinol medical applications, Mater. Sci. Eng. A. 275 (1999) 149–160. doi:10.1016/S0921-5093(99)00294-4.

[5] A.P. Stebner, D.W. Brown, L.C. Brinson, Young's modulus evolution and texture-based elastic–inelastic strain partitioning during large uniaxial deformations of monoclinic nickel–titanium, Acta Mater. 61 (2013) 1944–1956. doi:10.1016/J.ACTAMAT.2012.12.015.

[6] A. Stebner, X. Gao, D.W. Brown, L.C. Brinson, Neutron diffraction studies and multivariant simulations of shape memory alloys: Empirical texture development–mechanical response relations of martensitic nickel–titanium, Acta Mater. 59 (2011) 2841–2849. doi:10.1016/j.actamat.2011.01.023.

[7] M.F.-X. Wagner, W. Windl, Lattice stability, elastic constants and macroscopic moduli of NiTi martensites from first principles, Acta Mater. 56 (2008) 6232–6245. doi:10.1016/J.ACTAMAT.2008.08.043.

[8] S. Qiu, B. Clausen, S.A. Padula, R.D. Noebe, R. Vaidyanathan, On elastic moduli and elastic anisotropy in polycrystalline martensitic NiTi, Acta Mater. 59 (2011) 5055–5066. doi:10.1016/j.actamat.2011.04.018.

[9] S. Qiu, V.B. Krishnan, S. a. Padula, R.D. Noebe, D.W. Brown, B. Clausen, R. Vaidyanathan, Measurement of the lattice plane strain and phase fraction evolution during heating and cooling in shape memory NiTi, Appl. Phys. Let. 95 (2009) 141906. doi:10.1063/1.3245308.

[10] A.P. Stebner, D.W. Brown, L.C. Brinson, Measurement of elastic constants of monoclinic nickel-titanium and validation of first principles calculations, Appl. Phys. Let. 102 (2013). doi:10.1063/1.4808040.

[11] S. Rajagopalan, A.L. Little, M.A.M. Bourke, R. Vaidyanathan, Elastic modulus of shape-memory NiTi from in situ neutron diffraction during macroscopic loading, instrumented indentation, and extensometry, Appl. Phys. Let. 86 (2005) 081901. doi:10.1063/1.1863437.

[12] M. Thomasová, H. Seiner, P. Sedlák, M. Frost, M. Ševčík, I. Szurman, R. Kocich, J. Drahokoupil, P. Šittner, M. Landa, Evolution of macroscopic elastic moduli of martensitic polycrystalline NiTi and NiTiCu shape memory alloys with pseudoplastic straining, Acta Mater. 123 (2017) 146–156. doi:10.1016/j.actamat.2016.10.024.

[13] P. Šittner, L. Heller, J. Pilch, C. Curfs, T. Alonso, D. Favier, Youngs Modulus of Austenite and

Martensite Phases in Superelastic NiTi Wires, J. Mater. Eng. Perform. 23 (2014) 2303–2314. doi:10.1007/s11665-014-0976-x.

[14] N. Hatcher, O.Y. Kontsevoi, A.J. Freeman, Role of elastic and shear stabilities in the martensitic transformation path of NiTi, Phys. Rev. B. 80 (2009) 1–18. doi:10.1103/PhysRevB.80.144203.

[15] Y. Wang, J.J. Wang, H. Zhang, V.R. Manga, S.L. Shang, L.-Q. Chen, Z.-K. Liu, A first-principles approach to finite temperature elastic constants, J. Phys. Condens. Matter. 22 (2010) 225404. doi:10.1088/0953-8984/22/22/225404.

[16] J. Wang, H. Sehitoglu, Martensite modulus dilemma in monoclinic NiTi-theory and experiments, Int. J. Plast. 61 (2014) 17–31. doi:10.1016/j.ijplas.2014.05.005.

[17] J.B. Haskins, J.W. Lawson, Finite temperature properties of NiTi from first principles simulations: Structure, mechanics, and thermodynamics, J. Appl. Phys. 121 (2017) 205103–1.

[18] J.A. Monroe, D. Gehring, I. Karaman, R. Arroyave, D.W. Brown, B. Clausen, Tailored thermal expansion alloys, Acta Mater. 102 (2016) 333–341. doi:10.1016/j.actamat.2015.09.012.

[19] A. Ahadi, Y. Matsushita, T. Sawaguchi, Q.P. Sun, K. Tsuchiya, Origin of zero and negative thermal expansion in severely-deformed superelastic NiTi alloy, Acta Mater. 124 (2017) 79–92. doi:10.1016/j.actamat.2016.10.054.

[20] L. Zhang, D. Wang, X. Ren, Y. Wang, A new mechanism for low and temperature-independent elastic modulus, Sci. Rep. 5 (2015) 1–12. doi:10.1038/srep11477.

[21] Y.C. Xu, W.F. Rao, J.W. Morris, A.G. Khachaturyan, Nanoembryonic thermoelastic equilibrium and enhanced properties of defected pretransitional materials, Npj Comput. Mater. 4 (2018) 1–7. doi:10.1038/s41524-018-0114-7.

[22] Y. Wang, J. Gao, H. Wu, S. Yang, X. Ding, D. Wang, X. Ren, Y. Wang, X. Song, J. Gao, Strain glass transition in a multifunctional β-type Ti alloy., Sci. Rep. 4 (2014) 3995. doi:10.1038/srep03995.

[23] Multifunctional Alloys Obtained via a Dislocation-Free Plastic Deformation Mechanism (suupl), (n.d.) 8–13.

[24] T. Saito, T. Furuta, J.-H. Hwang, S. Kuramoto, K. Nishino, N. Suzuki, R. Chen, A. Yamada, K.

Ito, Y. Seno, T. Nonaka, H. Ikehata, N. Nagasako, C. Iwamoto, Y. Ikuhara, T. Sakuma, Multifunctional Alloys Obtained via a Dislocation-Free Plastic Deformation Mechanism., Science (80-.). 300 (2003) 464–467. doi:10.1126/science.1081957.

[25] W.-S. Ko, B. Grabowski, J. Neugebauer, Development and application of a Ni-Ti interatomic potential with high predictive accuracy of the martensitic phase transition, Phys. Rev. B. 92 (2015) 134107. doi:10.1103/PhysRevB.92.134107.

[26] G. Laplanche, T. Birk, S. Schneider, J. Frenzel, G. Eggeler, Effect of temperature and texture on the reorientation of martensite variants in NiTi shape memory alloys, Acta Mater. 127 (2017) 143–152. doi:10.1016/j.actamat.2017.01.023.

[27] S. Harjo, T. Ito, K. Aizawa, H. Arima, J. Abe, A. Moriai, T. Iwahashi, T. Kamiyama, Current Status of Engineering Materials Diffractometer at J-PARC, Mater. Sci. Forum. 681 (2011) 443–448. doi:10.4028/www.scientific.net/MSF.681.443.

[28] X. Jin, T. Nakamoto, S. Harjo, T. Hemmi, T. Umeno, T. Ogitsu, A. Yamamoto, M. Sugano, K. Aizawa, J. Abe, W. Gong, T. Iwahashi, Development of a cryogenic load frame for the neutron diffractometer at Takumi in Japan Proton Accelerator Research Complex, Rev. Sci. Instrum. 84 (2013) 1–5. doi:10.1063/1.4810010.

[29] A. Ahadi, T. Kawasaki, S. Harjo, W.-S. Ko, Q. Sun, K. Tsuchiya, Reversible elastocaloric effect at ultra-low temperatures in nanocrystalline shape memory alloys, Acta Mater. 165 (2019) 109–117. doi:10.1016/J.ACTAMAT.2018.11.035.

[30] R. Oishi-Tomiyasu, M. Yonemura, T. Morishima, A. Hoshikawa, S. Torii, T. Ishigaki, T. Kamiyama, Application of matrix decomposition algorithms for singular matrices to the Pawley method in {¥it Z-Rietveld}, J. Appl. Cryst. 45 (2012) 299–308. doi:10.1107/S0021889812003998.

[31] G. Kresse, J. Hafner, Ab initio molecular dynamics for liquid metals, Phys. Rev. B. 47 (1993) 558–561. doi:10.1103/PhysRevB.47.558.

[32] G. Kresse, J. Furthmüller, Efficient iterative schemes for ab initio total-energy calculations using a plane-wave basis set, Phys. Rev. B. 54 (1996) 11169–11186. doi:10.1103/PhysRevB.54.11169.

[33] J.P. Perdew, A. Zunger, Tools for Parallel Quantum Chemistry Software, Phys. Rev. B. 3 (2000) 67–96. doi:10.1103/PhysRevB.23.5048.

[34] J.P. Perdew, K. Burke, M. Ernzerhof, Generalized Gradient Approximation Made Simple (vol 77, pg 3865, 1996), Phys. Rev. Lett. 78 (1997) 1396–1396. doi:DOI 10.1103/PhysRevLett.78.1396.

[35] S. Baroni, S. De Gironcoli, A.D. Corso, S. Scuola, I. Superiore, I. Istituto, F. Materia, I.- Trieste, P. Giannozzi, Phonons and related crystal properties from density-functional perturbation theory, Rev. of. Mod. Phys. 73 (2001) 515–62. doi:10.1103/RevModPhys.73.515.

[36] X. Gonze, C. Lee, Dynamical matrices, Born effective charges, dielectric permittivity tensors, and interatomic force constants from density-functional perturbation theory, Phys. Rev. B. 55 (1997) 10355–10368. doi:10.1103/PhysRevB.55.10355.

[37] A. Togo, F. Oba, I. Tanaka, First-principles calculations of the ferroelastic transition between rutile-type and CaCl2-type SiO2at high pressures, Phys. Rev. B. 78 (2008) 1–9. doi:10.1103/PhysRevB.78.134106.

[38] A. Togo, I. Tanaka, First principles phonon calculations in materials science, Scr. Mater. 108 (2015) 1–5. doi:10.1016/j.scriptamat.2015.07.021.

[39] W.S. Ko, Temperature dependence of NiTi martensite structures: Density functional theory calculations, Scr. Mater. 154 (2018) 134–138. doi:10.1016/j.scriptamat.2018.05.037.

[40] M. Mizuno, H. Araki, Y. Shirai, Compositional dependence of structures of NiTi martensite from first principles, Acta Mater. 95 (2015) 184–191. doi:10.1016/j.actamat.2015.06.009.

[41] T. Shao, B. Wen, R. Melnik, S. Yao, Y. Kawazoe, Y. Tian, Temperature dependent elastic constants for crystals with arbitrary symmetry: Combined first principles and continuum elasticity theory, J. Appl. Phys. 111 (2012). doi:10.1063/1.4704698.

[42] B. Wen, T. Shao, R. Melnik, Y. Kawazoe, Y. Tian, Temperature and pressure dependent geometry optimization and elastic constant calculations for arbitrary symmetry crystals: Applications to MgSiO3perovskites, J. Appl. Phys. 113 (2013). doi:10.1063/1.4794360.

[43] W.-S. Ko, B. Grabowski, J. Neugebauer, Development and application of a Ni-Ti interatomic potential with high predictive accuracy of the martensitic phase transition, Phys. Rev. B. 92

(2015) 134107. doi:10.1103/PhysRevB.92.134107.

[44] F.J. Nye, Physical properties of crystals, Oxford University Press, Bristol, 1957.

[45] Y.P. Varshni, Temperature Dependence of Elastic Constants, Phys. Rev. B. 2 (1970) 3952. doi:10.1103/PhysRevB.2.3952.

[46] F. Bachmann, R. Hielscher, H. Schaeben, Texture Analysis with MTEX – Free and Open Source Software Toolbox, in: Solid State Phenom., Trans Tech Publications, 2010: pp. 63–68. doi:10.4028/www.scientific.net/SSP.160.63.

[47] L. Zhang, D. Wang, X. Ren, Y. Wang, A new mechanism for low and temperature-independent elastic modulus, Sci. Rep. 5 (2015) 11477. doi:10.1038/srep11477.

Figure captions

Fig. 1. Stress-strain responses of the polycrystalline martensitic NiTi specimens at three temperatures of 50, 150, and 50 K.

Fig. 2. (a) A photograph of the GM cryogenic loading frame mounted on the neutron diffractometer stage for *in situ* loading, (b) inside the GM cryogenic loading frame, (c) drawing of the dog-bone specimens used for *in situ* neutron diffraction experiments, and (d) the loading protocol and variations of the specimen's temperature in the course of collecting neutron spectra at 50 K.

Fig. 3 A typical no-load neutron diffraction spectra in the *d*-spacing range 1.4-3.3 Å recorded at 300 K, peaks indexed and numbered. Note that 012/111 peaks are completely overlapped and upon cooling they split. Thus, they are not included in the analyses. The peak 13 is an overlap of 003/022 peaks, however, the peak shows almost the same TE response as the 002 plane and does not split with cooling, thus it is indexed as 003.

Fig. 4. Thermal strain of 16 unique orientations of $B19'$ crystal with cooling down to 50 K and the corresponding three dimensional representation of the TE matrix (quadric) from, (a) our neutron diffraction experiments, (b) our QHA analysis, (b) DFT-MD results of Haskins et al. [17], and MEAM-MD results of Ko et al. [43].

Fig. 5. Evolution of the lattice strain ε_{hkl} with macroscopic applied stress σ_{macro}

perpendicular to 15 unique *hkl* planes of the B19′ crystal at three temperatures of 300, 150, and 50 K. The dashed lines are linear fits to the data points below 125 MPa for calculation of E_{hkl}.

Fig. 6. Variation of E (left axes) and ΔE (right axis) with cooling from 300 down to 50 K for 15 unique orientations perpendicular to *hkl* planes of the $B19'$ crystal. The dashed lines are exponential fits to the experimental data. The blue arrows point to the E_{hkl} at 150 K that a small elastic softening was detected.

Fig. 7. DFT-MD results of temperature-dependent elasticity of the $B19'$ crystal calculated with the $c_{ij}(T)$ provided in Ref. [17]. (a) Three dimensional representation surfaces (quadric)s of E_{hkl} at two temperatures of 300 and 50 K. The Y axis is parallel to b of $B19'$ crystal. The numbered surfaces are cross-section cuts through the quadric, (b) two dimensional plots of E_{hkl} corresponding to different cross-section cuts in (a) revealing the strong anisotropy of TDYM of $B19'$ crystal, (c) change in Young's modulus with temperature (ΔE vs T).

List of Tables

Table 1

Comparison between the measured orientation-dependent Young's modulus E_{hkl} at 300 K with the previous measurements in Ref. [8] and Ref. [10]. The Pearson linear correlation coefficient ρ is also indicated.

hkl	E_{hkl} (GPa)	ρ	E_{hkl} (Ref.[8])	$\left\|\frac{E_{hkl}-E_{hkl}^{Ref.[12]}}{E_{hkl}^{Ref.[12]}}\right\|$ (%)	E_{hkl} (Ref.[10])	$\left\|\frac{E_{hkl}-E_{hkl}^{Ref.[7]}}{E_{hkl}^{Ref.[7]}}\right\|$ (%)
011	113.1	0.9984	117.1	3.4	57.8	3.8
$10\bar{1}$	67.2	0.999	78.2	14	65.2	3
002	151	0.953	N/A	N/A	N/A	N/A
$11\bar{1}$	94.1	0.997	104.7	10.1	81.9	14.9
020	183.5	0.9962	N/A	N/A	55.6	230
$10\bar{2}$	84.6	0.9983	101.4	16.6	55.4	52
021	139.8	0.9234	145.4	3.8	50.8	175.2
$11\bar{2}$	86.6	0.9983	93.3	7.2	61.9	39.9
102	92.3	0.9981	N/A	N/A	NA	N/A
120	163.6	0.9995	167.1	2.1	NA	N/A
$12\bar{1}$	136	0.9977	165.1	17.6	75.3	80.6
112	94.9	0.9980	104.6	9.3	88.9	6.7
003	177.5	0.9949	N/A	N/A	62.6	183.5
$12\bar{2}$	102	0.9925	N/A	N/A	N/A	N/A

103	107.2	0.9871	N/A	N/A	N/A	N/A

Table 2

Comparison between the self-consistent (SC) model predictions with the room temperature neutron diffraction data of Ref. [8] and our 50 K neutron diffraction results.

hkl	E_{hkl} (GPa) 50 K	E_{hkl} (Ref.[8]) 300 K	E_{hkl} (Ref.[8]) SC model	$\left\|\frac{E_{hkl}^{model}-E_{hkl}^{50\,K}}{E_{hkl}^{50\,K}}\right\|$ (%)	$\left\|\frac{E_{hkl}^{model}-E_{hkl}^{300\,K}}{E_{hkl}^{300\,K}}\right\|$ (%)
011	131	117.1	155.7	18.8	33
$10\bar{1}$	75.9	78.2	105.1	38.5	34.4
$11\bar{1}$	112.1	104.7	130.2	16.1	24.4
$10\bar{2}$	91.2	101.4	106	16.2	4.5
021	166.4	145.4	146.7	11.8	0.9
$11\bar{2}$	93.9	93.3	122	29	30.8
120	185.7	167.1	152.8	17.7	8.6
$12\bar{1}$	152.1	165.1	147.6	2.9	10.6
112	136.5	104.6	116.3	14.8	11.2

Figure(1)
Click here to download high resolution image

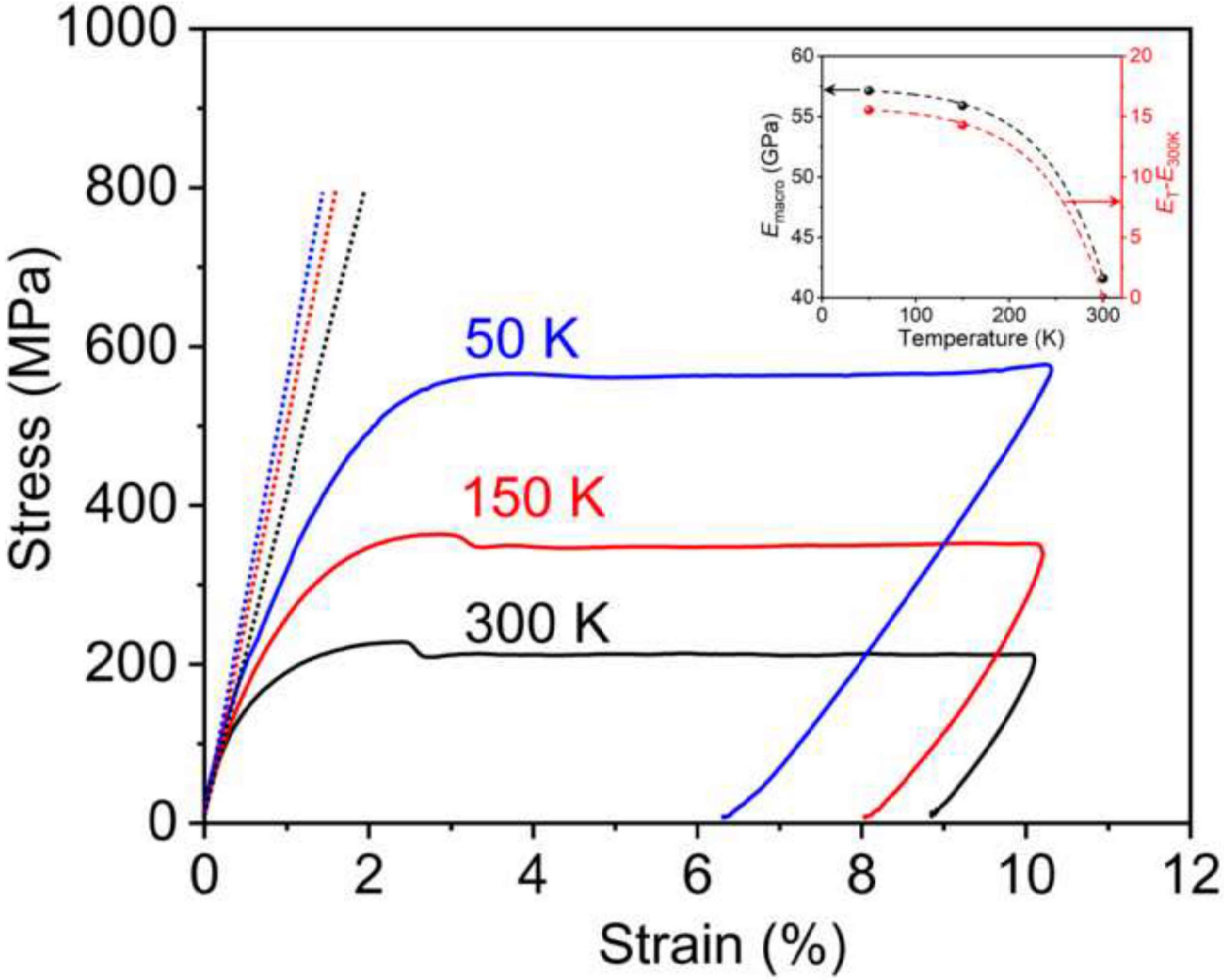

Figure(2)
Click here to download high resolution image

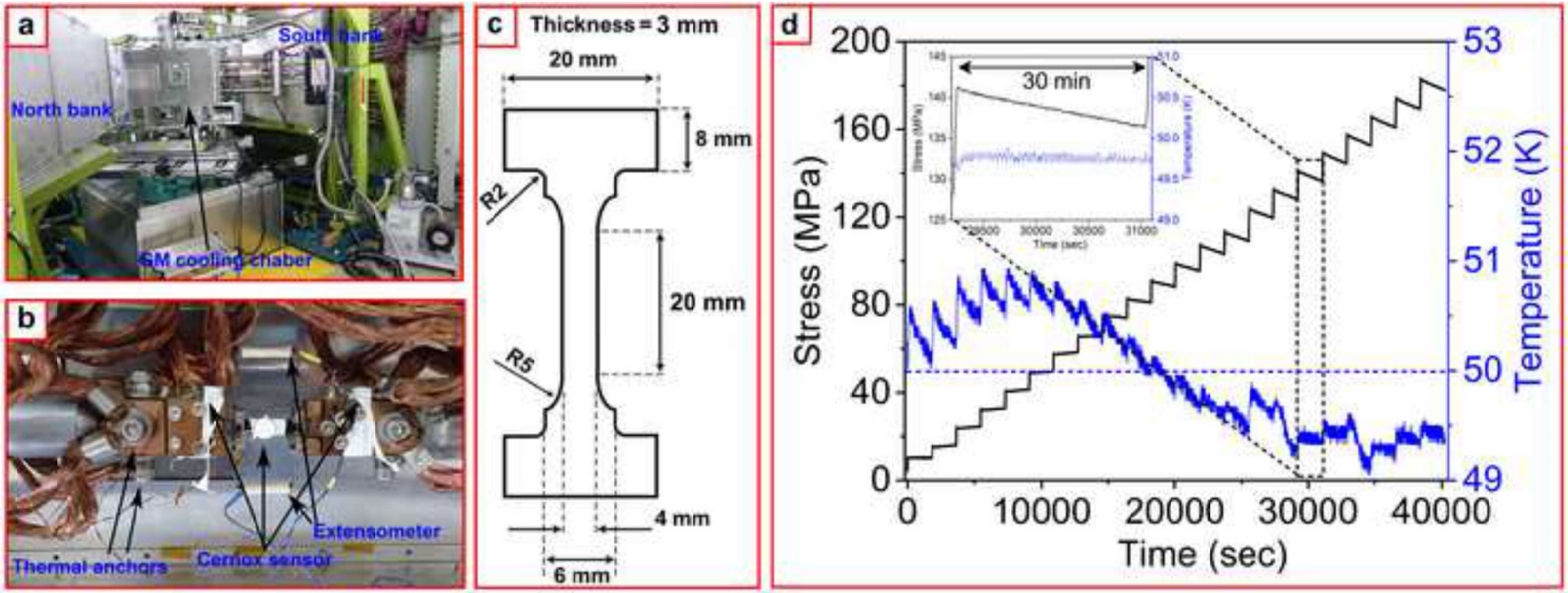

Figure(3)
Click here to download high resolution image

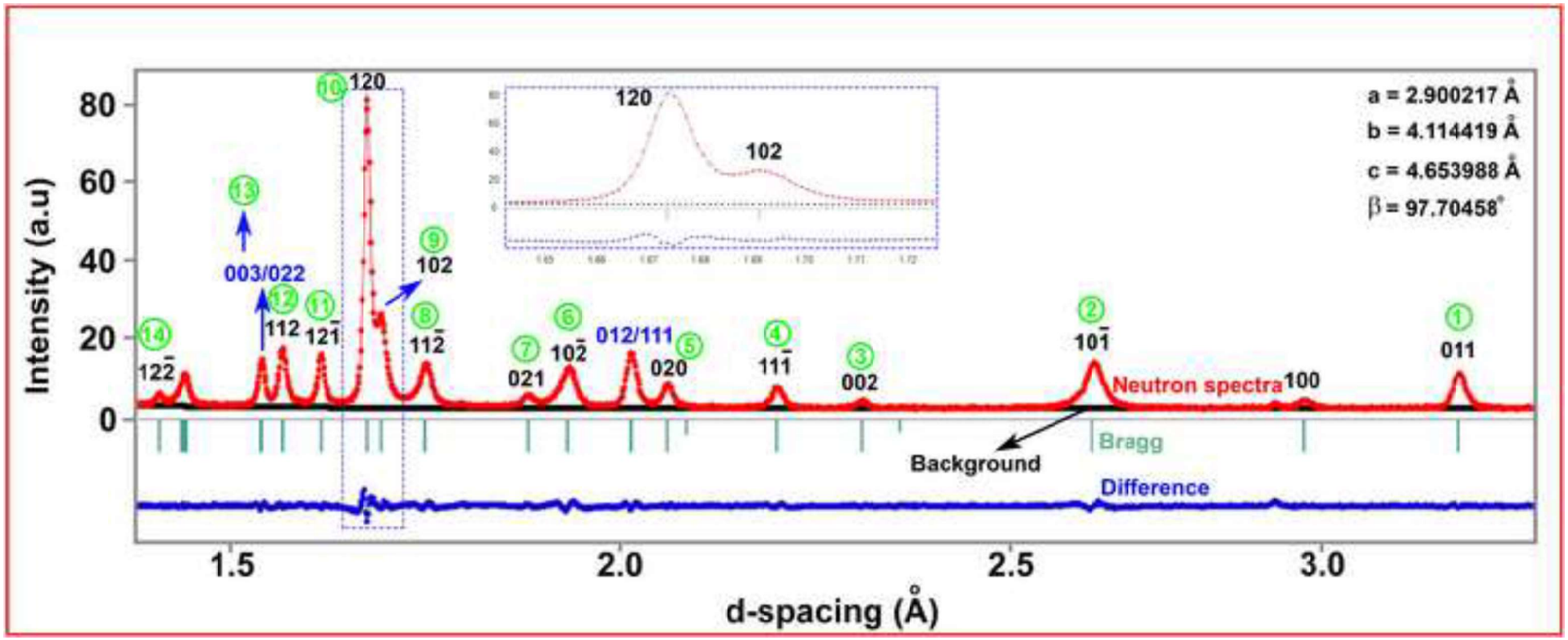

Figure(4)

Click here to download high resolution image

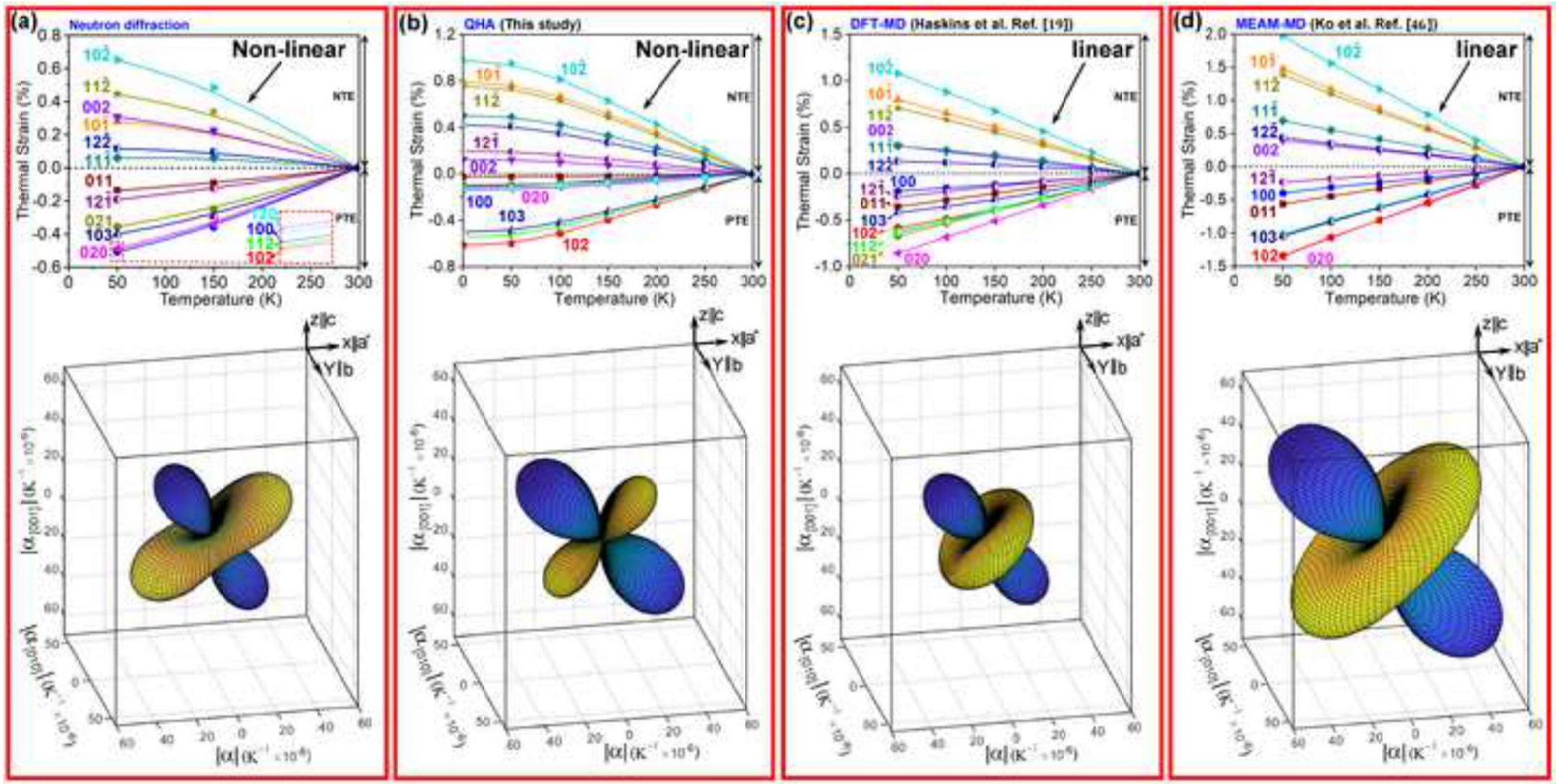

Figure(5)

Click here to download high resolution image

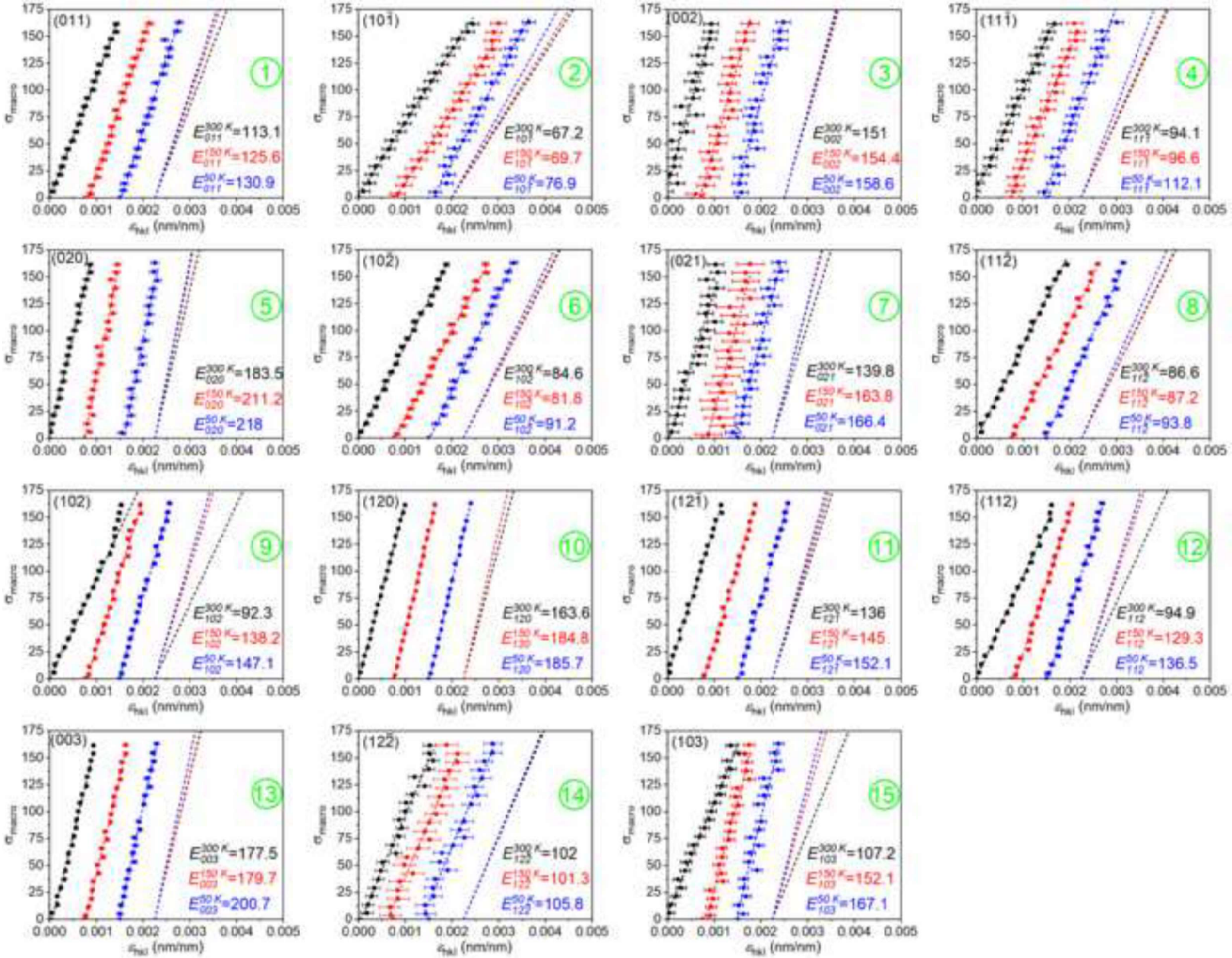

Figure(6)

Click here to download high resolution image

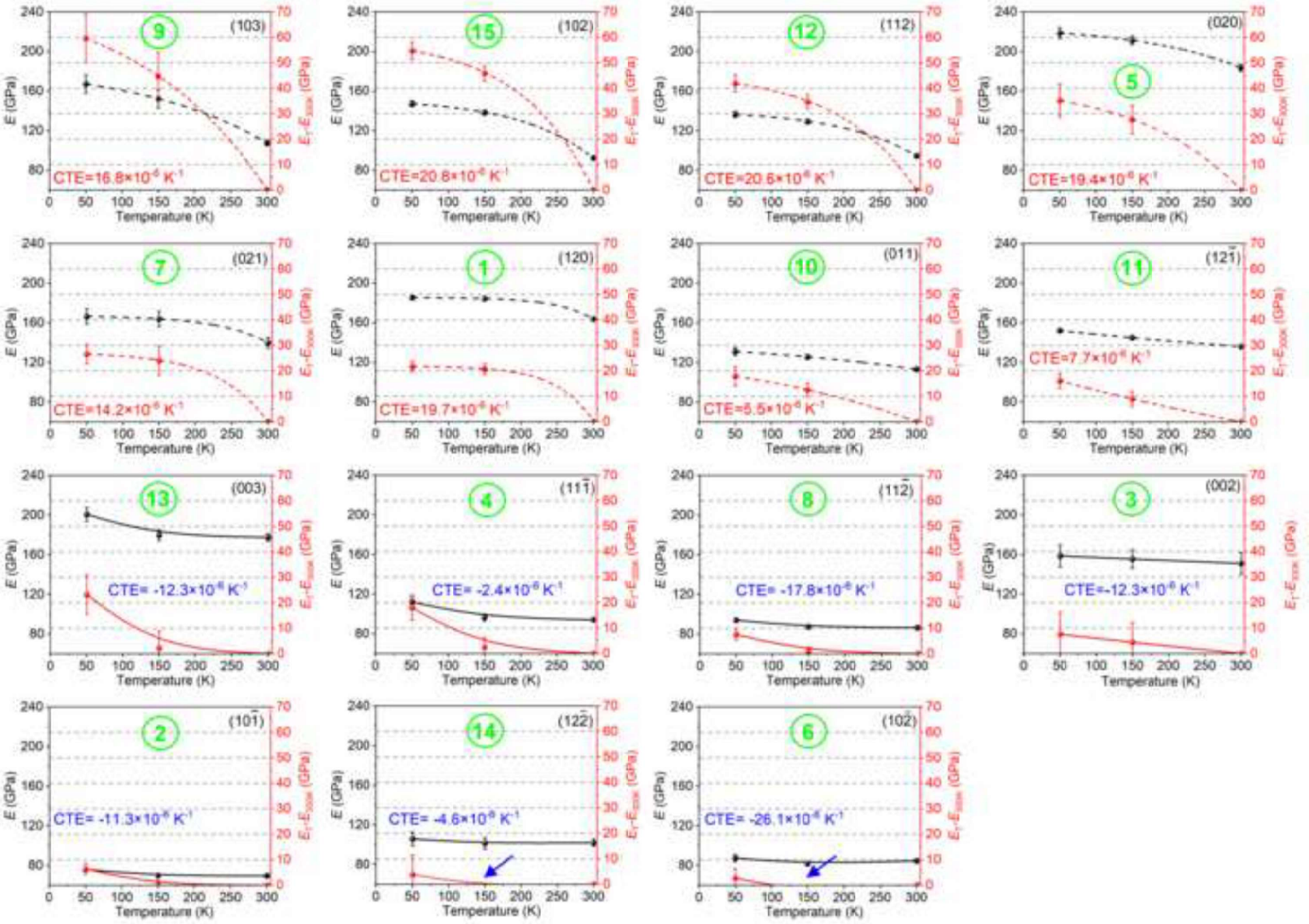

Figure(7)
Click here to download high resolution image

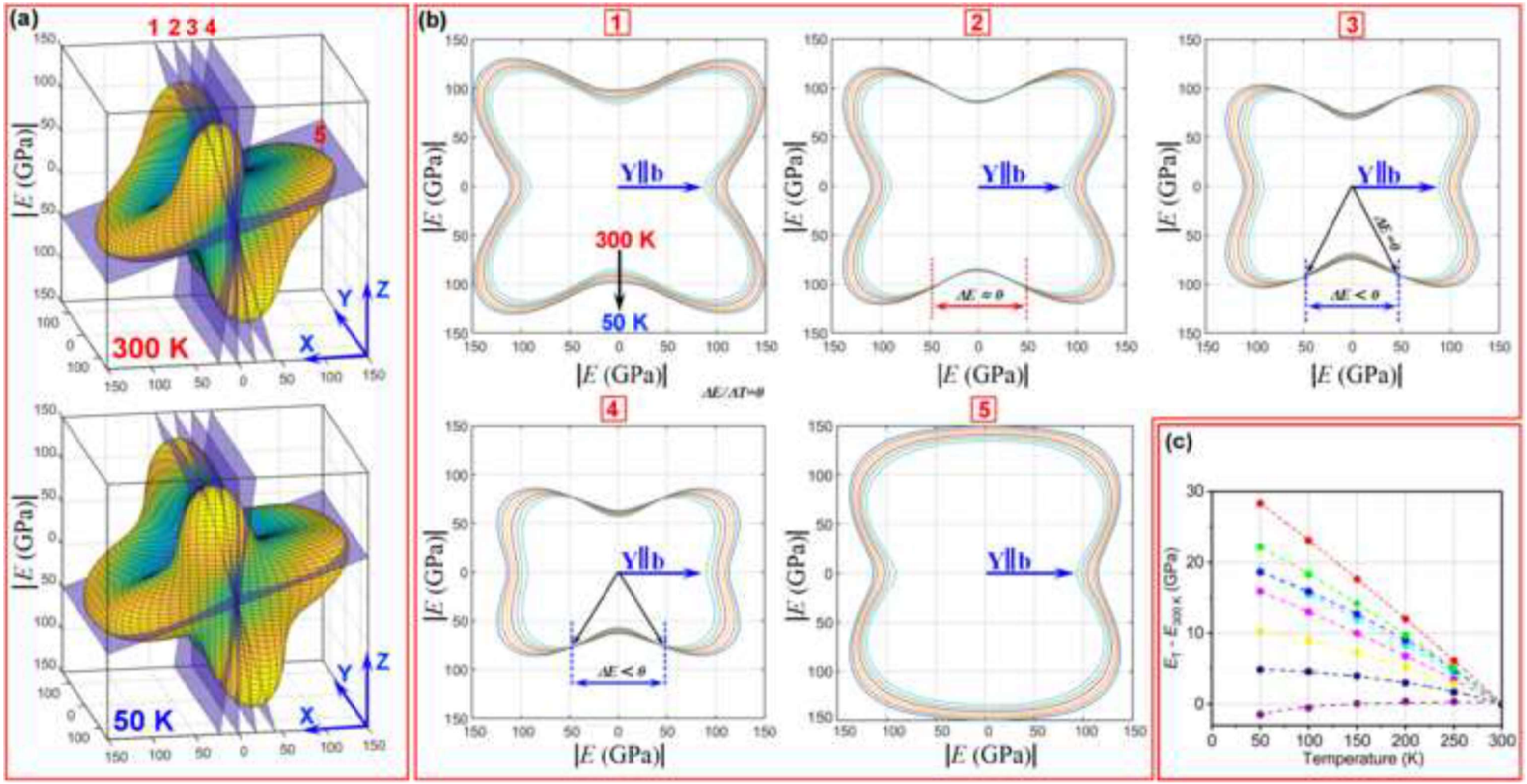

Supplementary Material

Click here to download Supplementary Material: F1.docx

*Graphical Abstract